Available online at www.sciencedirect.com

SciVerse ScienceDirect

Polar Science 7 (2013) 18–38

http://ees.elsevier.com/polar/

A spectral index ratio-based Antarctic land-cover mapping using hyperspatial 8-band WorldView-2 imagery

Shridhar D. Jawak*, Alvarinho J. Luis

National Centre for Antarctic and Ocean Research (NCAOR), Earth System Science Organization (ESSO, Ministry of Earth Sciences, Govt. of India, Headland Sada, Goa 403804, India

Received 19 May 2012; revised 20 November 2012; accepted 18 December 2012
Available online 2 January 2013

Abstract

This study evaluates the potential of 8-band high resolution WorldView-2 (WV-2) panchromatic (PAN) and multispectral image (MSI) data for the extraction of polar geospatial information. We introduce a novel method based on a customized set of normalized difference Spectral Index Ratios (SIRs), incorporating multiple bands, to improve the accuracy of land-cover mapping in the Antarctic. Most recently available WV-2 data are classified into land-cover surfaces such as snow/ice, water bodies, and landmass using the customized normalized difference SIRs. A novel multi-fold methodology is used to evaluate the effect of pan-sharpening algorithms on spectral characteristics of satellite data, and on subsequent land-cover mapping using an array of SIRs. A set of existing pan-sharpening algorithms was implemented in order to fuse PAN with MSI data, followed by estimation of multiple SIRs to extract target land-cover classes. These algorithms were compared on the basis of their effectiveness in extracting target classes using a defined set of SIRs. Our results indicate that the use of 8-band WV-2, customized SIRs, and appropriate pan-sharpening can greatly improve the extraction of land-cover information.

Keywords: Pan-sharpening; WorldView-2; Index ratios; Land-cover

1. Introduction

WorldView-2 (WV-2) is the first hyperspatial satellite that offers eight multispectral (MS) bands along with a panchromatic (PAN) band using imaging MS radiometers (VIS/IR) and a WV110 camera. The satellite, launched in October 2009, provides images at a spatial resolution of 0.50 m in the PAN band and 2 m in the MS bands. The Ground Sampling Distance (GSD) for the PAN band is about 0.46 m at nadir and 0.52 m at 20° off-nadir. For the eight MS bands, the GSD is about 1.80 m at nadir and 2.40 m at 20° off-nadir. The spatial resolution difference between PAN and MS modes can be measured by the ratio of their respective GSDs, which generally varies between 1:2 and 1:5; the GSD ratio for WV-2 is 1:4. The MS bands include four conventional visible and near-infrared bands common to multispectral satellites: Band 2, Blue (450–510 nm); Band 3, Green (510–580 nm); Band 5, Red (630–690 nm); and Band 7, Near-IR1 (NIR1) (770–895 nm), and four new bands: Band 1, Coastal (400–450 nm); Band 4, Yellow (585–625 nm); Band 6, RedEdge (705–745 nm); and

* Corresponding author. Tel.: +91 0 832 2525528; fax: +91 0 832 2520877.
E-mail addresses: shridhar.jawak@ncaor.org, shridhar.jawak@gmail.com (S.D. Jawak).

1873-9652/$ - see front matter © 2012 Elsevier B.V. and NIPR. All rights reserved.
http://dx.doi.org/10.1016/j.polar.2012.12.002

Band 8, Near-IR2 (NIR2) (860–1040 nm). These new channels enable access to spectral regions where distinguishable differences exist between multiple classifications within the scene, which may be overlooked by traditional MS systems such as Landsat 7.

The Spectral Index Ratio (SIR), which is used to classify a particular target or feature, is proportional to the difference in reflectance values of the bands used in the ratio. Traditionally, water and vegetation (Rouse et al., 1974) have been the primary focus of normalized difference SIRs, since water and vegetation are easy to discriminate on the basis of the difference in reflectance values in the range 450–750 nm.

Preliminary investigation on the bundled 8-band WV-2 imagery reveals a significant difference between the SIR images created using the 'traditional' spectral bands, equivalent to QuickBird's four spectral bands (Blue, Green, Red, and NIR1), and the 'new' WV-2 spectral bands. The existing SIRs used for effective land-cover mapping with WV-2 imagery are listed in Table 1. However, it is practically impossible to differentiate polar land-cover using just these two SIRs, as the landscape is very dynamic and consists of snow/ice of varying extent, texture, and morphology; landmasses of varying texture; and water bodies ranging from small ponds to large lakes. Also, the use of two simple SIRs underutilizes the 8-band capability of WV-2 data. We designed a novel set of normalized difference SIRs for WV-2 to fully exploit the 8-band capability. Each SIR includes at least one unique band from the set of newly available wavelengths. We focus our research efforts on designing new SIRs using the WV-2 acquisitions for Antarctic land-cover mapping.

The goal of the present paper is to demonstrate a new and simple method for mapping land-cover classes rapidly and accurately. Our study focuses on the following objectives: (a) to evaluate traditional pan-sharpening methods for WV-2 data on the basis of quality indices, (b) to design a "customized SIR" approach for 8-band WV-2 data to extract Antarctic land-cover and compare its performance with manually digitized land-cover map, and (c) to assess the unique 8-band characteristics of WV-2 data by employing multiple pan-sharpening algorithms coupled with multiple SIRs.

Table 1
List of existing normalized difference spectral index ratios (SIR).

Spectral index ratio	Spatial rationale	Mathematical expression	Reference
NDVI (Normalized Difference Vegetation index)	To extract vegetation	$\frac{NIR - Red}{NIR + Red}$	Rouse et al. (1974)
NDWI (Normalized Difference Water index)	To extract standing water	$\frac{Blue - NIR}{Blue + NIR}$	Gao (1996)

2. Literature review

Extensive research on image fusion techniques in Remote Sensing (RS) started in the late 1980s and early 1990s (Chavez et al., 1991; Cliche et al., 1985; Ehlers, 1991; Welch and Ehlers, 1987) and concentrated on pixel level fusion (pan-sharpening) in the late 1990s. Image fusion is the process of combining images of different resolution to increase the spectral and/or spatial quality of the fused image compared with the original (Pohl and Van Genderen, 1998; Wald et al., 1997). The fusion of RS images can assimilate the spectral information of a single sensor (Wang et al., 2005) or different sensors (Moser and Serpico, 2009). Fusion of the PAN and MS bands is classically referred to as pan-sharpening. Currently, pixel level image fusion is used as synonymous with pan-sharpening, resolution merge, image integration, or multi-sensor data fusion (Kumar et al., 2009; Vijayaraj et al., 2006). Today, a variety of airborne as well as space-borne sensors have produced image datasets of varying spatial, spectral and temporal resolution. Most of the Earth Observation (EO) satellites in operation, such as WorldView, Landsat, IRS-P5 (Cartosat), IRS 1C/1D, SAC-C, CBERS, SPOT, IKONOS, Quickbird, Formosat, and GeoEye, provide PAN images at a higher spatial resolution than in their MS mode. With the launch of these very high-resolution satellite sensors, the interest in pan-sharpening techniques has significantly increased. Much research has focused on preserving the spectral characteristics of the multispectral data after pan-sharpening (Alparone et al., 2007; Thomas et al., 2008).

Pan-sharpening techniques have become very important for RS applications such as enhancement of image classification, temporal change detection studies, object identification and selection, image segmentation, map updating, and enhanced visualization (Yuhendra et al., 2012). Various pan-sharpening algorithms have been developed (Ranchin and Wald, 2000; Ranchin et al., 2003; Wang et al., 2005), and some have been incorporated in commercial RS software packages such as ERDAS 9.3 and ENVI 4.8 (Ehlers et al., 2010; Shah et al., 2008). Most of these methods work well with images that were acquired at

the same time by one sensor (single-sensor, single-date fusion) (Alparone et al., 2007; Ehlers, 2008). Generally, image fusion methods can be classified into three levels: pixel level, feature level, and decision level. Pixel level image fusion techniques have the highest relevance for RS applications, as the data are least altered and most of the pan-sharpening techniques have been developed for this type of fusion (Wald et al., 1997; Zhang, 2004).

Recently, Amro et al. (2011) provided a detailed review of the classical and state-of-the-art pan-sharpening methods described in the literature, and they suggested a clear classification of various pan-sharpening methods and gave a detailed description of their main characteristics. Most of the fusion methods developed for improving spatial and spectral resolutions of RS images are based on Intensity–Hue–Saturation (IHS) (Choi, 2006), Color Normalization (CN) Brovey (Bovolo et al., 2010), multiresolution analysis such as High Pass Filter (HPF) (Wald et al., 1997), and Principal Component Analysis (PCA) (Shah et al., 2008). Other methods such as Gram–Schmidt (GS) (Kumar et al., 2009), CN-spectral (Vrabel et al., 2002), and Ehlers fusion (Ehlers et al., 2010) are based on intensity modulation. PCA and GS are based on component substitution featuring the construction of a generalized intensity as a linear combination of the MS bands. In addition, several researchers have proposed the use of a wavelet transform (cf. Shi et al., 2005) or discrete wavelet transform (Li et al., 2005) to extract geometric edge information from PAN images. In particular, wavelet techniques led to a number of new fusion methods (Otazu et al., 2005; Yunhao et al., 2006). Thomas et al. (2008) provided a critical review of these fusion methods based on RS physics and pointed out the weaknesses and strengths of each method.

It is necessary to provide a general assessment of the quality of the sharpened images for their potential use in the present application. Thus, one of the main purposes of this study is to assess six commonly employed pan-sharpening methods in terms of their ability to preserve the spectral information provided in the MS image, and to examine their final effect on SIR-based mapping accuracy. Visual inspection coupled with a quantitative approach based on the evaluation of spectral and spatial distortion due to fusion is more desirable for mathematical modeling (Li et al., 2010; Vijayaraj et al., 2006). Wald et al. (1997) formulated a protocol to test the quality of fused images. In this work, we employ six evaluation measures to compare the pan-sharpening: the Universal Image Quality Index (UIQI) (Wang and Bovik, 2002), Structural Similarity Index (SSIM) (Wang et al., 2004), Spectral Angle Mapper (SAM) (Thomas and Wald, 2007), Erreur Relative Globale Adimensionnelle de Synthèse (ERGAS, relative dimensionless global error in synthesis) (Wald, 2000), Zhou's spatial correlation index/ High-pass Correlation Coefficient (HCC) (Zhou et al., 1998), and the Correlation Coefficient (CC) (Zhang, 2008).

Different techniques have been employed to map land-cover, such as using indices derived from the RS images. A commonly used Normalized Difference Vegetation Index (NDVI) involves calculation of the difference between the reflectance values in the NIR and red channels normalized by their sum. Achard and Estréguil (1995) used multitemporal AVHRR mosaics for tropical forest mapping with NDVI. Fernandez et al. (1997) mapped the surfaces affected by large forest fires using NDVI. The Normalized Difference Snow Index (NDSI), derived from Landsat Thematic Mapper (TM) bands 2 and 5 [(TM2 − TM5)/(TM2 + TM5)], has been successfully used to map glaciers (Sidjak and Wheate, 1999). NDSI is based on the difference between the strong reflection of visible radiation and near total absorption of middle infrared wavelengths by snow (Hall et al., 1995a, 1995b). It is effective in distinguishing snow from 'bright' surfaces such as soil, vegetation, rock, and clouds (Dozier, 1989). The Normalized Difference Water Index (NDWI) can be used as the SIR for water class extraction, identifying water bodies, and discriminating natural and man-made features (Ben-Dor et al., 2001). The NDWI, defined as (Green − NIR)/(Green + NIR), was developed to delineate open water features and enhance their presence in RS imagery on the basis of reflected near-infrared and visible green wavelengths (McFeeters, 1996). NDWI is sensitive to changes in the liquid water content of vegetation canopies, so it is complementary to, but not a substitute for, NDVI (Gao, 1996).

These indices were designed for traditional medium resolution V–NIR systems, and have not been validated for the 8-band WV-2 data for Antarctic land-cover mapping. WV-2 provides a duplet of V–NIR bands, and presents an opportunity to customize a new set of SIRs to support Antarctic land-cover mapping. The present study differs from previous studies based on reconsideration and reconstruction of SIRs for 8-band WV-2 data for land-cover mapping.

3. Data

3.1. Description of remotely sensed image data

We used radiometrically corrected, georeferenced, orthorectified 16-bit standard level 2 (LV2A) WV-2 multi-sequence images acquired on 10 September 2010 at an off-nadir angle of 1.95° over the Larsemann Hills, East Antarctica. The data consist of 9 tiles of 8-band MS and PAN images. These tiles were spatially mosaicked to generate a single continuous image.

The WV-2 image covers an area of 100 km^2 with different land-cover (snow, ice, rocks, lakes, permafrost, *etc*.), and with flat, hilly and mountainous terrain, resulting in a range of heights from 5 to 700 m. The period of satellite data acquisition corresponds to the beginning of austral spring in Antarctica, when solar radiation reaches the surface on clear days.

3.2. Description of multitemporal field reference and existing map data

Remote sensing data cannot be used efficiently without ground truth, especially for polar studies. The ground truth datasets used to support land-cover mapping include data from the Antarctic Data Centre (AADC), the Indian Scientific Expedition to Antarctica (InSEA), historical Google Earth images and pan-sharpened WV-2 images.

Extensive mapping work has been carried out by the AADC in the last few decades (http://www.aad.gov.au/) and by teams participating in the InSEA since 2005. An important resource of land-cover data for the Larsemann Hills is the AADC "Larsemann Hills Photogrammetric Mapping Project" (Harris, 2008). A large-scale mapping of the Larsemann Hills (1:2500 scale) was carried out by the Survey of India from September 2007 to February 2008. These maps were digitized to extract land-cover data. Historical Google Earth images acquired on 31 December 1999, 24 February 2006, 3 March 2006, and 4 January 2011 were used to identify the land-cover classes and to crosscheck the multitemporal snow-cover statistics over the study area. Considering the high spatial resolution of WV-2 data itself, various land-cover classes can be extracted manually from the pan-sharpened images.

Based on prior knowledge of the study area and visual analysis of the satellite data, the WV-2 GS-sharpened image was manually digitized using ArcGIS 10 to extract a land map consisting of the three land-cover classes of interest: snow/ice, water, and landmass. An accurate area was calculated for each land-cover class using the GIS routines. Since this manually digitized map of the study area was generated based on prior knowledge of its geography and on the WV-2 image, we consider the generated land-cover database a reliable basis for accuracy assessment. The location map of the study area and the map of manually extracted and digitized land-cover are shown in Figs. 1 and 2, respectively.

Three land-cover classes were extracted to yield a land-cover map of the Larsemann Hills region, east Antarctica between 76°03′39″E, 69°21′49″S and 76°18′54″E, 69°27′10″S. The Larsemann Hills are a series of low rounded, snow-free coastal hills along the southeast shore of Prydz Bay. There are over 150 lakes in the Larsemann Hills, ranging from small shallow ponds less than 1 m deep to glacial lakes up to 38 m deep, with area varying between 100 and 33,000 m^2.

4. Methodology

The data processing protocol implemented for this land mapping application is shown in Fig. 3. The steps consist of four blocks: (i) data preprocessing (calibration), (ii) data fusion and evaluation of pan-sharpening, (iii) land-cover feature extraction and land map generation, and (iv) accuracy evaluation.

The data processing was carried out as follows. First, a dark pixel subtraction was applied to the dataset to make best use of the dynamic range. Second, pan-sharpening of the WV-2 MS image was performed

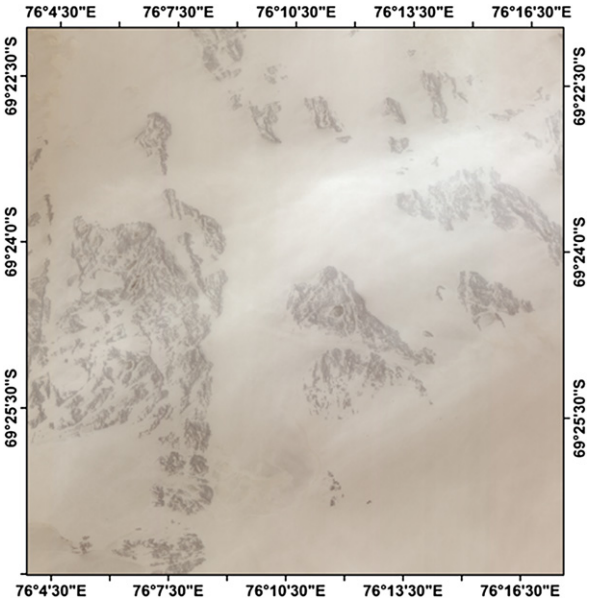

Fig. 1. Location map of study area (source: WV-2 MSI).

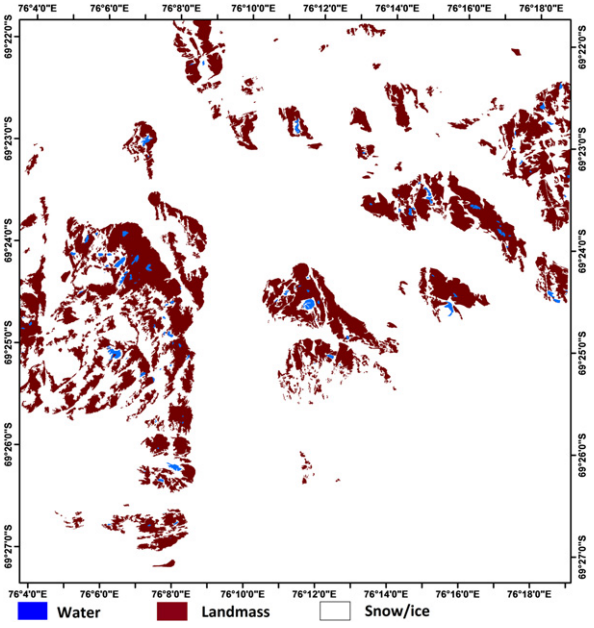

Fig. 2. Manually extracted/digitized land-cover map of the study area.

using the standard fusion methods available in ERDAS 9.3 and ENVI 4.8. These fusion methods were assessed for spectral and spatial quality of the pan-sharpened images. Finally, to evaluate the influence of pan-sharpening on land-cover mapping, a new set of normalized SIRs with specific band combinations was generated. Each SIR was calculated for all the pan-sharpened images, and output images were generated for all SIRs. The resultant individual images were stacked into one final land map dataset. Each fusion method produced a single land-cover map.

5. Image processing

Each block of the methodology (Fig. 3) is discussed as follows.

5.1. Data preprocessing: WorldView-2 calibration

The calibration information in a metadata file (XML) of the WV-2 imagery was used to calibrate WV-2 by applying the WorldView calibration utility (ENVI 4.8). The calibration method was adapted from the literature (Updike and Comp, 2010).

5.2. Shadow minimization effect

Because of the high resolution of WV-2 images with respect to contextual information, the shadow minimization effect with or without contextual information was applied to minimize the global posterior energy function, using following equation (Tso and Mather, 2001):

$$U(\mu/\boldsymbol{d}) = (1-\lambda)U(\boldsymbol{d}/\mu) + \lambda U(\mu), \quad (1)$$

where $U(\mu/\boldsymbol{d})$ is global posterior energy function, $U(\boldsymbol{d}/\mu)$ is the conditional energy function, and $U(\mu)$ is the prior energy function, λ is the smoothness parameter that controls the balance between the two energy functions and its value ranges between 0 and 1.

5.3. Data fusion and evaluation of pan-sharpening

5.3.1. Pan-sharpening

In the present study, the PAN and MSI are captured at the same time with the same sensor. Thus, pan-sharpening can be carried out directly without further registration. In order to create clutter at a resolution of 0.50 m, the multiband image was pan-sharpened from a resolution of 2.00 m–0.50 m. Six pan-sharpening algorithms available in ENVI 4.8 and ERDAS IMGINE 9.3, including PCA (Chavez et al., 1991), Brovey Transform (BT) (Hallada and Cox, 1983), Wavelet-based Principle Component (W-PC) (Pradhan et al., 2006), Ehlers Fusion (EF) (Klonus and Ehlers, 2007), Gram Schmidt (GS) (Laben and Brower, 2000), and High Pass Filtering (HPF) (Schowengerdt, 1980) were employed. All the six pan-sharpening methods were implemented using default/standardized settings available in ERDAS 9.3 (ERDAS, 2010) and ENVI 4.8 (ENVI, 2011). To ensure unbiased quality evaluation, the default settings were not optimized for individual pan-sharpening methods.

The statistics for the sharpened images were then calculated using IDL 7 and Matlab 4 routines. After pan-sharpening, the quality of the fusion product based on each fusion method is examined by visual and statistical analysis. To illustrate our findings in the following section, we use a subset of the WV-2 image, as it represents the different fusion effects. Fig. 4 depicts the original multispectral WV-2 (Band 5, Red; Band 3, Green; and Band 2, Blue) and the PAN image along with the sharpened images. Since the performance of these algorithms is spectrally and spatially dependent, an evaluation of the spectral and spatial quality of the pan-sharpened images was undertaken using quality metrics.

5.3.2. Evaluation of pan-sharpening

Currently there is no consensus in the literature (Li, 2000) on the best quality index for pan-sharpening. The protocol proposed by Wald et al. (1997) offers

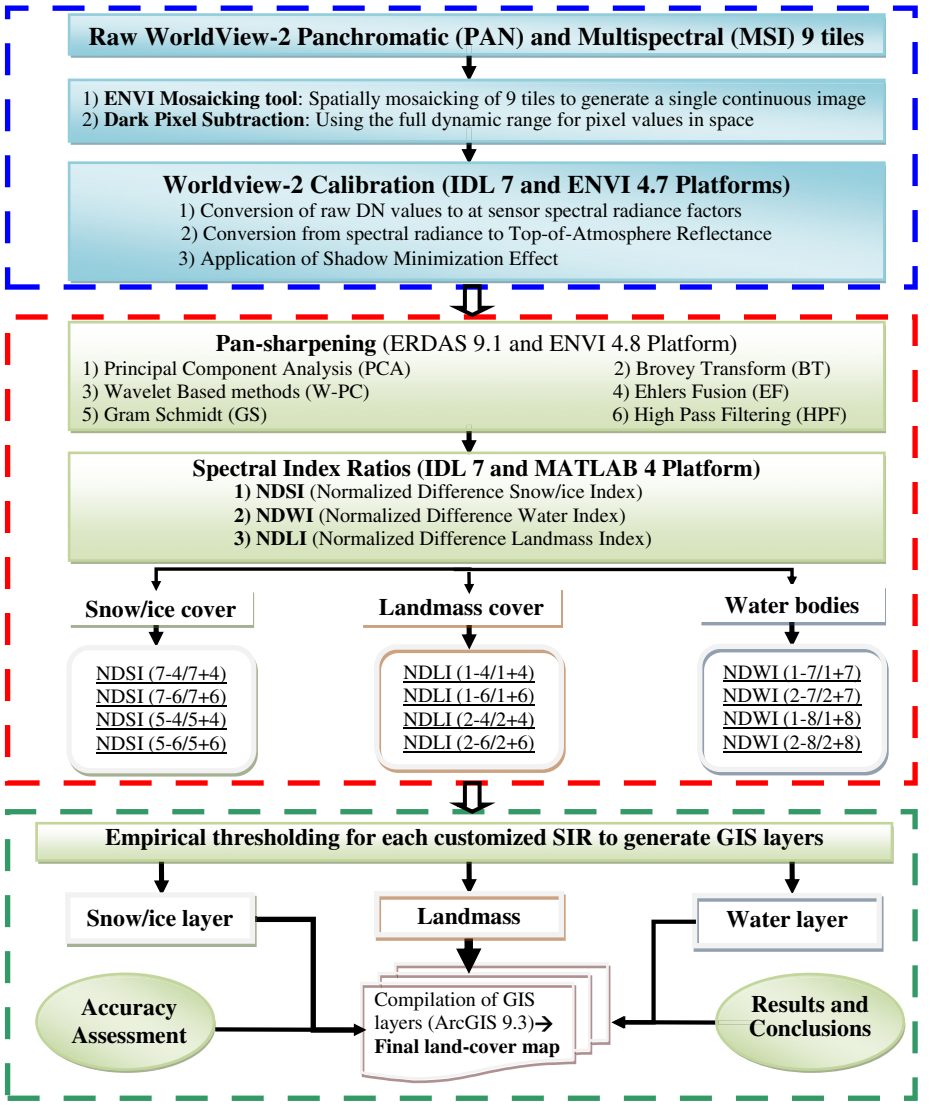

Fig. 3. Methodology adopted for land-cover mapping.

a robust approach to the assessment of quality. A number of statistical evaluation methods are used to measure post-fusion color fidelity. These methods should be objective, reproducible, and of a quantitative nature. Therefore, we selected the following statistical measures.

(i) Wang and Bovik (2002) proposed the Universal Image Quality Index (UIQI)/(Wang–Bovik index), Q_{WB}, defined as:

$$Q_{WB} = \frac{4\mathrm{cov}(x,y)E(x)E(y)}{\left[\left(\mathrm{var}(x)+\mathrm{var}(y)\right)\left(E(x)^2+E(y)^2\right)\right]}, \qquad (2)$$

where $E(x)$ represents the mean of x (original image), $E(y)$ represents the mean of y (fused image), $\mathrm{cov}(x,y)$ corresponds to the covariance of x and y, and $\mathrm{var}(x)$ and $\mathrm{var}(y)$ are the variance of x (original image) and y (fused image), respectively. In order to apply the Q_{WB} quality index, a reference image is needed. This presents a problem for pan-sharpening since no reference image exists at the pan-sharpened resolution. In order to compute Q_{WB}, we downsampled the pan-sharpened image to the original MS resolution, which allowed us to compute the quality index directly. The index can be computed at a specified scale or block size, and varies between −1 and 1, with 1 representing the best quality. Following Padwick et al. (2010), we used a block size of

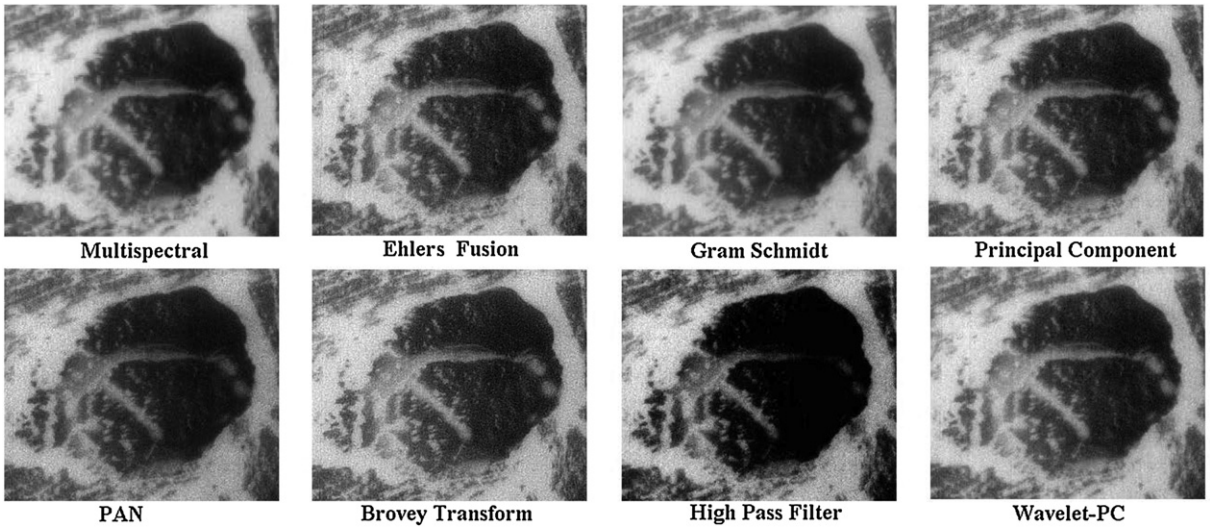

Fig. 4. Original WV-2 multispectral and PAN images along with sharpened images.

approximately ¼ of the image. The Q_{WB} index was computed for each band in the original MSI, producing a vector of values. We define the quantity $\mathbf{Q}_{\lambda}$ for the eight MS bands as follows.

$$\mathbf{Q}_{\lambda} = [Q_{WB}(MS_1, PS_1), Q_{WB}(MS_2, PS_2)\ldots. \times Q_{WB}(MS_8, PS_8)], \quad (3)$$

where MS indicates the original MS band and PS indicates the pan-sharpened band (downsampled to the MS resolution).

(ii) The objective of this study is to find the fused image with the optimal combination of spectral characteristic preservation and spatial improvement. The literature has mostly concentrated on spectral consistency, with little or no emphasis on spatial improvement. To avoid this shortcoming, we selected a widely used high-pass (HP) spatial correlation index to measure the quality of spatial improvement. For the calculation of the High-pass Correlation Coefficient (HCC), an HP filter with a 3 × 3 Laplacian kernel was first applied to the PAN image and to each band of the fused image. Then the correlation coefficients between the HP filtered bands and the HP filtered PAN image were calculated. This analysis was first proposed by Zhou et al. (1998).

The HCC of two signals A and B is defined as:

$$\mathrm{HCC}(A,B) = \frac{\sum(Ai - \mu A)(Bi - \mu B)}{\sqrt{\sum(Ai - \mu A)^2 (Bi - \mu B)^2}}, \quad (4)$$

where μ_A and μ_B are the means of signals A and B, respectively, and the summation runs overall elements i of each signal. The HCC metric varies from −1 to +1. $\mathbf{HCC}_{\lambda}$ for an 8-band MSI can be defined as:

$$\mathbf{HCC}_{\lambda} = [\mathrm{HCC}(Pan, PS_1), \mathrm{HCC}(Pan, PS_2)\ldots \times \mathrm{HCC}(Pan, PS_8)], \quad (5)$$

where Pan indicates the PAN band and PS indicates the pan-sharpened band, with the subscript indicating the band index. The statistics of the Q_{WB} and HCC indices are summarized in Table 2.

(iii) The structural similarity (SSIM) index was proposed by Wang et al. (2004). The SSIM is a further development of the Q_{WB} index, and is widely used to assess the spectral value preservation of pan-sharpened images (Alparone et al., 2004). This method, which combines a comparison of luminance, contrast, and structure, was applied locally on an 8 × 8 pixel window. This window was moved pixel-by-pixel over the entire image. At each pixel, the local statistics and the SSIM index were calculated within the window. The values vary between 0 and 1, with values close to 1 indicating the highest correspondence with the original image.

$$\mathrm{SSIM} = \frac{(2E(x)E(y) + c1)(2\mathrm{cov}(x,y) + c2)}{\left[\left(E(x)^2 + E(y)^2 + c1\right)\left(\mathrm{var}(x) + \mathrm{var}(y) + c2\right)\right]}, \quad (6)$$

where $c1 = (k_1 L)^2$, $c2 = (k_2 L)^2$, L is the dynamic range of pixel values, $k_1 = 0.01$, and $k_2 = 0.03$. $E(x)$ represents

Table 2
Quantitative evaluation of pan-sharpening on the basis of Q_{WB} and HCC indices.

WV-2 spectral details		Pan-sharpening algorithms											
Band name	Wavelength (nm)	EF		BT		HPF		GS		W-PC		PC	
		HCC	Q_{WB}	HCC	Q_{WB}	HCC	Q_{WB}	HCC	Q_{WB}	HCC	Q_{WB}	HCC	Q_{WB}
Coastal	400–450	0.770	0.922	0.772	0.682	0.598	0.616	0.924	0.997	0.815	0.925	0.832	0.923
Blue	450–510	0.836	0.975	0.837	0.786	0.685	0.714	0.938	0.993	0.847	0.976	0.846	0.975
Green	510–580	0.869	0.993	0.870	0.854	0.745	0.778	0.946	0.999	0.878	0.998	0.869	0.993
Yellow	585–625	0.874	0.996	0.875	0.992	0.770	0.904	0.949	0.999	0.875	0.999	0.880	0.999
Red	630–690	0.872	0.997	0.873	0.913	0.783	0.832	0.952	0.990	0.873	0.998	0.877	0.998
RedEdge	705–745	0.866	0.997	0.867	0.933	0.792	0.851	0.954	0.988	0.887	0.998	0.866	0.999
NIR1	770–895	0.848	0.993	0.849	0.959	0.794	0.875	0.956	0.983	0.864	0.995	0.858	0.994
NIR2	860–1040	0.827	0.991	0.828	0.986	0.797	0.899	0.961	0.983	0.838	0.994	0.838	0.990
	Average	0.845	0.983	0.846	0.888	0.746	0.809	0.948	0.992	0.860	0.985	0.858	0.984
Correlation coefficient		0.926		0.698		0.953		−0.651		0.837		0.737	

the mean of x (original image), $E(y)$ represents the mean of y (fused image), cov(x,y) is the covariance of x and y, while var(x) and var(y) are the variance of x (original image) and y (fused image), respectively.

(iv) The correlation coefficient (CC) between the original MS bands and the corresponding fused bands is the most frequently used method to evaluate the preservation of spectral value (Klonus and Ehlers, 2007; Zhang, 2008). Its value ranges from −1 to 1. The best correspondence between fused and original image data shows the highest correlation value 1. The statistics of the SSIM and CC indices are summarized in Table 3.

(v) ERGAS (relative dimensionless global error in synthesis) is a normalized version of the root mean square error (RMSE) designed to calculate spectral distortion. ERGAS is commonly used to assess the quality of pan-sharpened images. This index measures distortion and must be as small as possible. ERGAS is defined as,

$$\mathrm{ERGAS} = \frac{100h}{l}\sqrt{\frac{1}{N}\sum_{i=1}^{N}\frac{\mathrm{RMSE}^2(\mathrm{Bi})}{\mathrm{Mi}^2}}, \tag{7}$$

where $\mathrm{RMSE}^2(Bi) = \mathrm{Bias}^2(\mathrm{Bi}) + \mathrm{SD}^2(\mathrm{Bi})$, h and l are the resolution of PAN and MS, respectively, Mi represents the mean radiance of each spectral band involved, Bi represents the MS bands, SD represents the standard deviation, Bias represents the difference between arithmetic means of MSI and fused image, and N is the total number of spectral bands.

(vi) SAM (Spectral Angle Mapper) has been widely used in MS or hyperspectral image analysis to measure the spectral similarity of substance signatures for material identification. A SAM value equal to zero denotes the absence of spectral distortion, but radiometric distortion may be present. SAM is measured either in degrees or in radians and is usually averaged over the whole image to yield a global measurement of spectral

Table 3
Quantitative evaluation of pan-sharpening on the basis of CC and SSIM indices.

WV-2 spectral details		Pan-sharpening algorithms											
Band name	Wavelength (nm)	EF		BT		HPF		GS		W-PC		PC	
		CC	SSIM	CC	SSIM	CC	SSIM	CC	SSIM	CC	SSIM	CC	SSIM
Coastal	400–450	0.793	0.550	0.795	0.522	0.633	0.461	0.942	0.731	0.831	0.621	0.854	0.628
Blue	450–510	0.853	0.561	0.856	0.529	0.715	0.451	0.953	0.751	0.867	0.641	0.863	0.64
Green	510–580	0.891	0.554	0.893	0.532	0.761	0.468	0.969	0.741	0.894	0.637	0.887	0.632
Yellow	585–625	0.890	0.543	0.891	0.521	0.792	0.469	0.967	0.742	0.893	0.631	0.903	0.635
Red	630–690	0.896	0.548	0.894	0.527	0.801	0.473	0.974	0.748	0.898	0.639	0.898	0.633
RedEdge	705–745	0.885	0.561	0.882	0.515	0.807	0.461	0.973	0.757	0.917	0.641	0.881	0.637
NIR1	770–895	0.862	0.559	0.862	0.520	0.812	0.458	0.977	0.748	0.874	0.642	0.877	0.621
NIR2	860–1040	0.851	0.549	0.845	0.529	0.813	0.457	0.987	0.737	0.868	0.623	0.852	0.637
	Average	0.865	0.553	0.865	0.524	0.767	0.462	0.968	0.744	0.880	0.634	0.877	0.633

distortion. SAM is defined as the angular difference between two spectral vectors, ***S1*** and ***S2***, according to following equation,

$$\mathrm{SAM}(\mathrm{S1},\mathrm{S2}) = \arccos\left(\frac{\mathrm{S1}.\mathrm{S2}}{\|\mathrm{S1}\|.\|\mathrm{S2}\|}\right) \quad (8)$$

The statistics of the ERGAS and SAM indices are summarized in Table 4.

5.4. Land-cover feature extraction

All the six pan-sharpened WV-2 images were subjected to an integrated SIR-based land-cover mapping approach, which consists of the following steps.

5.4.1. Workflow for designing customized SIRs

Customized SIRs were empirically evaluated through spectral profile observations. The spectral responses of representative pixels in the three land-cover classes were calculated, and averaged within classes to provide a spectral profile. Visual inspection of the profiles identified the most useful bands for discriminating each class. A sample profile illustrates that three classes have greatest spectral disparity for different bands (Supplementary Fig. 1). The maximum and minimum response bands were then normalized to yield the normalized difference target class index (NDCI) (Fig. 5). The procedure was time consuming for the eight-band image, given the number of individual responses considered.

Close scrutiny of spectral profiles reveals that snow/ice covered areas have highest reflectance in band 7 and lowest in band 4. However, it is also evident that these areas have considerable spectral disparity between bands 5 and 6. Similar inferences were drawn on the basis of such profiles for the other two land-cover classes.

Fig. 5 shows the workflow for generating a custom target class SIR, *i.e.,* NDCI. It is a time consuming-process for WV-2 data, because of its high spatial and spectral resolution compared with other datasets. We note that the NDCI does not maximize the response of a specific class, but best discriminates the target class from other regions in the image.

Table 4
Quantitative evaluation of pan-sharpening on the basis of SAM and ERGAS indices.

Method	EF	BT	HPF	GS	W-PC	PC
SAM	0.598	0.613	0.649	0.403	0.492	0.557
ERGAS	0.293	0.326	0.437	0.207	0.218	0.235

5.4.2. Designing SIRs for present study

In this section, we discuss the procedure and the need for customization of existing SIRs used in the present study (*i.e.*, NDSI, NDWI, and NDLI), based on the workflow (Fig. 5) and existing literature. Customized SIRs proposed using WV-2 imagery to establish an effective land-cover map are listed in Table 5.

5.4.2.1. Customization of NDWI. Huggel et al. (2002) developed the NDWI by normalizing the blue band against the NIR band, since the difference in response is very obvious. In our experiment the coastal band is normalized by the NIR2 band. Since the difference in response of each of these unique bands is greater, it creates a discrete threshold for detecting areas of standing water (Table 5). NDWI produces a single grayscale image, where water appears bright. Some other features may also appear bright, such as buildings and clouds. However, the possibility of buildings having a spectral response similar to that of water in the study area is remote. Since the satellite image was acquired under minimum cloud cover conditions, standing water is the only feature that appears bright on the NDWI image. The data acquisition period represents the beginning of austral spring when solar radiation initiates ice melting in Antarctica. Melt water on ice surfaces will have a similar spectral response since NDWI discriminates water from other land-cover classes. To differentiate melt water, it is necessary to threshold the NDWI value, so that the overall region can be classified as target class (water bodies) or non-target (snow, rocks and melt water) classes.

5.4.2.2. Customization of NDSI. The existing shortwave infrared (SWIR) band-based NDSI is analogous to the NDVI (Tucker, 1979) and is useful for identifying and discriminating snow/ice from most cumulus clouds. The NDSI is generally used for snow-cover mapping using satellite data (Hall et al., 1995a), based on the high and low reflectance of snow in the visible (Green) and SWIR regions, respectively, yielding the ratio (Green − SWIR)/(Green + SWIR).

Since there is no SWIR band available on WV-2, it was necessary to customize the NDSI for our analysis. From spectral profile analysis (Supplementary Fig. 1),

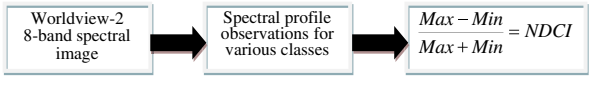

Fig. 5. Workflow for generating a customized Normalized Difference Class Index (NDCI).

Table 5
List of customized SIRs: Mathematical expressions and their threshold settings.

		Threshold range
Normalized difference landmass index		
NDLI $_{(1\ -\ 4/1\ +\ 4)}$	$\frac{\text{Coastal} - \text{Yellow}}{\text{Coastal} + \text{Yellow}}$	0.201–0.673
NDLI $_{(1\ -\ 6/1\ +\ 6)}$	$\frac{\text{Coastal} - \text{RedEdge}}{\text{Coastal} + \text{RedEdge}}$	0.221–0.689
NDLI $_{(2\ -\ 4/2\ +\ 4)}$	$\frac{\text{Blue} - \text{Yellow}}{\text{Blue} + \text{Yellow}}$	0.213–0.671
NDLI $_{(2\ -\ 6/2\ +\ 6)}$	$\frac{\text{Blue} - \text{RedEdge}}{\text{Blue} + \text{RedEdge}}$	0.224–0.687
Normalized difference water index		
NDWI$_{(1\ -\ 7/1\ +\ 7)}$	$\frac{\text{Coastal} - \text{NIR1}}{\text{Coastal} + \text{NIR1}}$	0.641–0.788
NDWI$_{(2\ -\ 7/2\ +\ 7)}$	$\frac{\text{Blue} - \text{NIR1}}{\text{Blue} + \text{NIR1}}$	0.671–0.871
NDWI$_{(1\ -\ 8/1\ +\ 8)}$	$\frac{\text{Coastal} - \text{NIR2}}{\text{Coastal} + \text{NIR2}}$	0.640–0.773
NDWI$_{(2\ -\ 8/2\ +\ 8)}$	$\frac{\text{Blue} - \text{NIR2}}{\text{Blue} + \text{NIR2}}$	0.668–0.863
Normalized difference snow/ice index		
NDSI $_{(7\ -\ 4/7\ +\ 4)}$	$\frac{\text{NIR1} - \text{Yellow}}{\text{NIR1} + \text{Yellow}}$	0.404–0.831
NDSI $_{(7\ -\ 6/7\ +\ 6)}$	$\frac{\text{NIR1} - \text{RedEdge}}{\text{NIR1} + \text{RedEdge}}$	0.414–0.843
NDSI $_{(5\ -\ 4/5\ +\ 4)}$	$\frac{\text{Red} - \text{Yellow}}{\text{Red} + \text{Yellow}}$	0.411–0.881
NDSI $_{(5\ -\ 6/5\ +\ 6)}$	$\frac{\text{Red} - \text{RedEdge}}{\text{Red} + \text{RedEdge}}$	0.423–0.787

it is evident that there are differences in the response values of snow/ice between the NIR1–Yellow, NIR1–RedEdge, Red–Yellow, and Red–RedEdge band pairs; this specific band information has been exploited to represent snow in this study (Table 5). The customized NDSI approach is an effective way to distinguish snow from other surface features.

5.4.2.3. Customization of NDLI. The NDLI is used to identify areas where soils and rocks are the dominant background or foreground material. Normally, SWIR and NIR bands are used to represent the difference in reflectance values for soil/rock areas. There is no SWIR band in WV-2, but there are characteristic differences in the response values for soil in the Coastal–Yellow, Coastal–RedEdge, Blue–Yellow, and Blue–RedEdge bands. This spectral information has been exploited to represent landmass (Table 5). Drawing from a sample of the landmass within the scene, a consistent and unique difference between the customized NDLI bands was observed, which was constant for all landmass regions (Supplementary Fig. 1). All detections were validated by cross-referencing the signatures in corresponding regions in the true and false color composites with the detections in the NDLI. This is a remarkable new method for determining areas of soil/rock content without using a SWIR band.

5.4.3. Threshold technique

After customization, the defined set of SIRs was applied to the values in the radiance cube for the six pan-sharpened images, and output images were generated for each SIR. The difference between the response values in the SIR determines where the respective classes such as snow/ice, landmass and water are located on the scene. Once these areas were identified from the SIR images, the optimal threshold values were set to capture only the feasible regions of classification (Table 5).

The threshold technique is important in SIR-based classification and is expressed as:

$$T = T[x, y, p(x, y), f(x, y)], \tag{9}$$

where T is the threshold value; x, y are the coordinates of the threshold value point; $p(x, y)$ is the probability distribution of the pixel located in the xth column and yth row of the SIR image and $f(x, y)$ is the value of the pixel located in the xth column and yth row of the SIR image. The threshold image $g(x, y)$ can be defined as:

$$\begin{aligned} g(x,y) &= 1, \quad \text{if } f(x,y) > \mathrm{T} \\ &= 0, \quad \text{if } f(x,y) \le \mathrm{T} \end{aligned} \tag{10}$$

The threshold values for the present study were empirically evaluated by repeated manual scrutiny of the most obvious 100 pixels (per target class) from SIR images derived from the eight pan-sharpened images. The same 100 pixel locations were scrutinized for all the pan-sharpened SIR images to ensure unbiased accuracy analysis. Pixels with a SIR value higher than the local threshold were assigned 1 (target class pixels), while pixels with a lower SIR value than the local threshold were assigned 0 (non-target class pixels). The ranges of threshold values for various SIR combinations for all pan-sharpened images are summarized in Table 5. The threshold used for each SIR was kept constant for all the pan-sharpening algorithms to ensure unbiased comparison and assessment of accuracy.

5.5. Land-cover map generation

In this experiment, we designed four customized modifications for three SIRs to differentiate three land-cover classes. Hence, each class is eventually classified

by four customized SIRs (Table 5). Each customized SIR identifies the desired class with varying success, on the basis of the bands used for designing that SIR and the threshold set for identifying the desired class. For instance, considering NDWI, some lakes could be identified by one combination of bands, while other combinations could not reveal those lakes. It is also possible that some lakes could be identified by more than one NDWI band combination. Hence, it was necessary to merge all the individual NDWI combinations to avoid redundancy and to yield a composite output map of water (NDWI). This also applies to the other two classes.

The SIR output maps produced from each pan-sharpened image were layered into a final land-cover dataset. The final land-cover map was generated by synergistic merging of the three output SIR maps for each pan-sharpening algorithm. This is our novel step, implementing a second additional GIS-based fusion of SIR maps to generate a final land-cover map.

The land-cover classes obtained were vectorized to generate ArcGIS-compatible shapefiles, which were used to calculate the land-cover class area. The multifold flowchart for processing WV-2 to generate individual SIR maps and the subsequent final land-cover map is depicted in Fig. 6. All the pan-sharpened images were processed in a similar way to generate final output maps.

5.6. Accuracy assessment

We assessed the results of our land-cover extraction approach by visual interpretation and statistical measures.

5.6.1. Visual analysis

We displayed the original MSI, the manually digitized land-cover map, and the resultant SIR-based land-cover maps in three display windows. By overlaying ground truth-based polygon layers of manually digitized land-cover maps on the SIR-based land-cover map layers, visual interpretation was carried out satisfactorily.

5.6.2. Error matrices

According to the widely used rule "number of bands (8) × number of classes (3) × 10", a minimum 240 validation test points are necessary to calculate the accuracy of the land-cover map. However, given the image size and number of classes, a set of 240 points was not considered as a statistically significant sample. The accuracy assessment of all output land-cover maps was therefore carried out using a stratified random selection of 3000 test points to ensure an approximately equal distribution of points among the three land-cover classes. We used the most commonly employed "error matrices" for accuracy assessment of

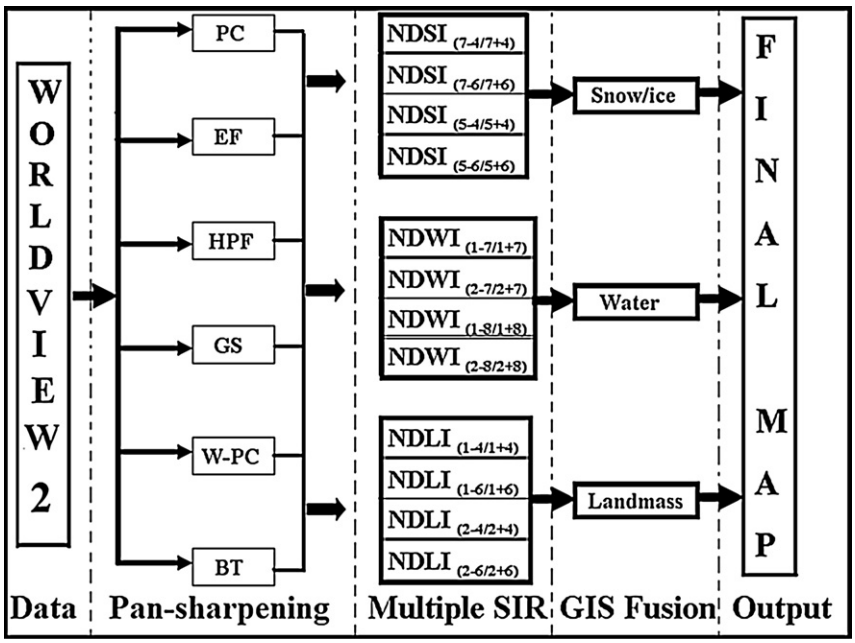

Fig. 6. Processing flowchart for analysis of WV-2 data to produce a land-cover map.

land-cover maps (Congalton, 1991), such as pixels classified correctly for the entire map, errors of inclusion (commission), errors of exclusion (omission), user's accuracy, producer's accuracy, overall accuracy, mean accuracy and kappa coefficient of agreement.

5.6.3. Statistical analysis

Very accurate pre-digitized land-cover area data for the three classes were used as the reference for evaluating the accuracy of all the SIR-based land-cover maps. The areas of all the three classes were estimated from the vectorized outputs of SIR-based land-cover maps. In the last step, a statistical comparison was made between manually pre-digitized land-cover area and SIR-based classified land-cover area for all the three classes using bias and root mean square error (RMSE).

The bias for each extracted class is defined as:

$$\text{Bias} = \text{Ar}_i - \text{Am}_i, \tag{11}$$

where Am_i is the ith original area value measured using SIR-based land-cover classification, Ar_i is the reference value from the manually digitized land-cover map, and n is the number of land-cover classes. The average and percentage bias were calculated to evaluate the final accuracy.

To quantify the uncertainty of our analysis, we calculated the RMSE using:

$$\text{RMSE} = \sqrt{\frac{1}{n}\sum_{i=1}^{n}(\text{Ar}_i - \text{Am}_i)^2} \tag{12}$$

6. Results

We offer a few comments on the methodology. In the first step, the performance and quality of pan-sharpening techniques of high-resolution RS images from WV-2 were evaluated. In the second step, quantitative analysis of the pan-sharpened image was carried out. In the third step, a customized SIR-based method was developed to extract land-cover classes. In the final step, the accuracy was evaluated on the basis of RMSE and bias of land-cover area derived using the customized SIR approach.

6.1. Quantitative evaluation of pan-sharpening algorithms

The process of pan-sharpening introduces a variety of spectral and spatial distortions, which may affect the subsequent land-cover mapping. Hence, a quantitative quality evaluation was necessary before the actual implementation of the customized SIRs. The results of evaluation of this pan-sharpening based on quantitative indices are shown in Tables 2–4 and summarized in Supplementary Table 1. A set of six traditional algorithms (EF, PC, BT, HPF, GS, and W-PC) was compared on the basis of Wald's protocol. A value approaching 1 for all indices (except SAM and ERGAS) indicates very good performance.

The SSIM and Q_{WB} values are useful for evaluating the similarity between the sharpened image and the original image. SSIM and Q_{WB} consider the similarity of two images on the basis of three different factors; namely, loss of correlation, radiometric distortion, and contrast distortion. A higher SSIM index value indicates greater similarity between the fused image and the original MSI. In Tables 2 and 3 we compare the SSIM and Q_{WB} values for sharpened and original images. Both values show that the GS-sharpened images are closer to the original MSI than the other five sharpening methods. As shown in Tables 2 and 3, the GS ($Q_{WB} = 0.992$, SSIM = 0.744) method yields the best results, while the HPF ($Q_{WB} = 0.809$, SSIM = 0.462) and BT ($Q_{WB} = 0.888$, SSIM = 0.524) methods yield comparatively poorer results in a given cohort. In contrast, the W-PC ($Q_{WB} = 0.985$, SSIM = 0.634), EF ($Q_{WB} = 0.983$, SSIM = 0.553) and PC ($Q_{WB} = 0.984$, SSIM = 0.633) methods yield almost equivalent results with minor variations.

The spectral performance of the algorithms can be ranked quantitatively in terms of Q_{WB} and SSIM (Supplementary Table 1) as GS > W-PC > PC > EF > BT > HPF. The trend indicates that the GS algorithm performed best while the HPF performed worst of the set of six algorithms. However, we note that the values of CC, SSIM, and Q_{WB} for W-PC and PC are comparable since the W-PC algorithm models the input bands slightly better than PC. Also note that the SAM and ERGAS values for W-PC exceeded that of PC, indicating that the difference was not caused by variation in either spectral or spatial quality, but was due to the overall performance of the algorithm.

A high HCC value indicates that most of the spatial information from the PAN image is incorporated in the sharpened image. Table 2 presents the HCC calculated between the sharpened image and the PAN image. The GS method (HCC = 0.948) yields the best result, while the HPF (HCC = 0.746) yields the poorest result in a given cohort. This shows that the GS-sharpened

images have higher spatial correlation, which indicates that more information from the PAN image is incorporated in the sharpened image. On the other hand, EF (HCC = 0.845) and BT (0.846) are almost equivalent in performance. Similarly, W-PC (HCC = 0.860) and PC (HCC = 0.858) perform equally well in the spatial context. The HCC index based (spatial quality) ranking can be summarized as GS > W-PC > PC > BT > EF > HPF. Based on spatial considerations (HCC), the trend reveals that the BT method performed better than the EF, which is the reverse of the spectral situation (Q_{WB}, SSIM). The spatial quality for the EF algorithm was lower than that for BT, with the coastal band lower (HCC = 0.770), but the spectral quality was superior (Q_{WB} = 0.922). This suggests that the poor spatial performance was offset by the excellent spectral performance.

The SAM, CC, and ERGAS values indicate the spectral quality of the sharpened image. As shown in Tables 3 and 4, it is evident that the GS method (SAM = 0.403, CC = 0.968 and ERGAS = 0.207) yields the best results, while the HPF (SAM = 0.649, CC = 0.767 and ERGAS = 0.437) yields the poorest results in a given cohort. The spectral performance of the algorithms can be ranked quantitatively in terms of SAM and ERGAS, (Supplementary Table 1) as GS > W-PC > PC > EF > BT > HPF. Interestingly, BT and EF have the same CC index value (0.865), indicating the comparable spectral performances for these algorithms.

The GS algorithm is the sharpest algorithm (highest score), retaining spectral and spatial quality much better than other algorithms, while the HPF algorithm scored the lowest among the six algorithms. In brief, from a spectral point of view, we conclude that GS performs best, closely followed by W-PC, PC, EF, BT, and HPF. However, from a spatial point of view, GS is much superior to the other algorithms. We also computed the correlation between the indices of spatial quality (HCC) and spectral quality (Q_{WB}) (Table 2), which indicates that the correlation is positive for all pan-sharpening algorithms except for GS. The negative correlation suggests that the poor spatial performance was offset by excellent spectral performance for the GS algorithm.

In brief, the analysis of quality measures following Wald's protocol indicates that the GS algorithm maintained the best balance between spectral and spatial quality so as to preserve consistency and synthesis properties more efficiently than the other sharpening methods, and hence surpassed the performance of the other pan-sharpening algorithms.

6.2. SIR performance

Each ratio produced realistic results with areas of noticeable similarity as evident in both the true/false color composites of the original data and in the classification regions within the land-cover map. The Larsemann Hills region is situated on the eastern coast of Antarctica, where the sea-ice and snow-cover extent varies significantly from summer to winter. The current acquisition captured only a few water bodies ranging from shallow ponds to deep lakes, which provide a similar response to the NDWI. The clear detection of standing water validates the theory that the coastal band is a unique variable in the NDWI equation. In the second phase of validation, the same process was run again using the blue band instead of the coastal band. As a result, the threshold had to be increased to filter out a larger number of false alarms, showing that the coastal band is superior to the traditional blue band for evaluating the NDWI. This is not surprising, as in many cases the response of the coastal band was greater than that of the blue band in areas of standing water. However, out of 109 manually digitized water bodies, the NDWI approach could successfully extract only 97 water bodies in the final land-cover map. A visual analysis revealed that the missing water bodies were very small in size, typically 130–200 m^2 in area. We infer that the NDWI method failed to extract small water bodies because they were in a semi-frozen state, so these might have been misclassified as ice/snow since the optimum threshold ranges could not extract them. A set of twelve missing water bodies is shown on Supplementary Fig. 2. A final NDWI map obtained from the GS-sharpened image is shown in Fig. 7.

Presently, the use of the Yellow and the NIR1 bands was not adequate to classify areas of snow/ice cover. With WV-2 imagery, the NDSI can be calculated using either the NIR1–Yellow/RedEdge or Red–Yellow/RedEdge bands. The advantage of having the Yellow band is that the difference in the response values between the two regions (NIR1–Yellow and Red–Yellow) is even greater, thereby widening the threshold for positive classifications of snow/ice. We found that some rocky terrain, which was partially covered by snow/ice, had NDSI values similar to that of snow/ice cover. Hence, these were separated from snow/ice cover using the NDSI computed with the RedEdge band. In contrast, other surfaces had NDSI (RedEdge) values similar to that of snow/ice cover but were separable using the NDSI values calculated with the NIR1 or Red band. Most of these pixels appeared at the edges of rocky terrain or shadowed rocky areas. In

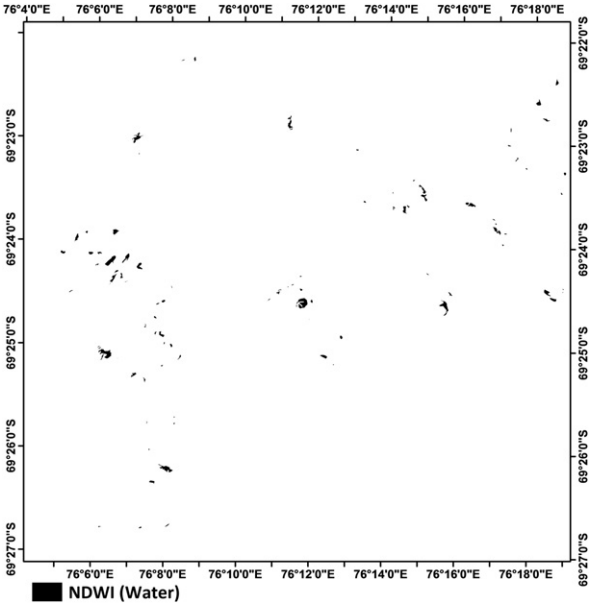

Fig. 7. Resultant merged NDWI map compiled from GS-sharpened image.

brief, we infer that the combined use of the four NDSI values enabled a much more accurate separation of snow/ice cover from other classes (Fig. 8).

Landmass features are often the simplest to extract from homogeneous backgrounds, but in our scenario the background comprised different types of materials such as fully exposed rocks, partially snow-covered rocks and landmass surrounded by water bodies. However, the performance of the NDLI was outstanding, with detection of not only the most obvious landmass materials (fully exposed rocks), but also partially snow-covered landmass and even obscure static objects such as land surrounded by lakes. The use of the red edge and coastal bands to detect natural hard surfaces (NDLI) was a success (Fig. 9). This is the second most abundant layer in the resulting land-cover map.

However, in the case of NDLI the spectral distortions caused by the pan-sharpening algorithm resulted in a varying degree of misclassification of snow/ice pixels as landmass pixels at the edges of rocky terrain in all the six pan-sharpened images. An example of such a misclassification, an HPF-sharpening-based land-cover map, is shown in Supplementary Fig. 3. Interestingly, this misclassification is significantly reduced in the GS-sharpened image (Fig. 9).

6.3. Comparative assessment of pan-sharpening on the basis of error matrices

A multi-sequence and bi-fusion (two merging steps) methodology ensured reliability in the generation of accurate land-cover maps from each pan-sharpened image. Each pan-sharpening method yielded three SIR-based GIS layers: NDSI, NDLI, and NDWI. In turn, each SIR was calculated using four different band combinations. Twelve GIS layers from each pan-

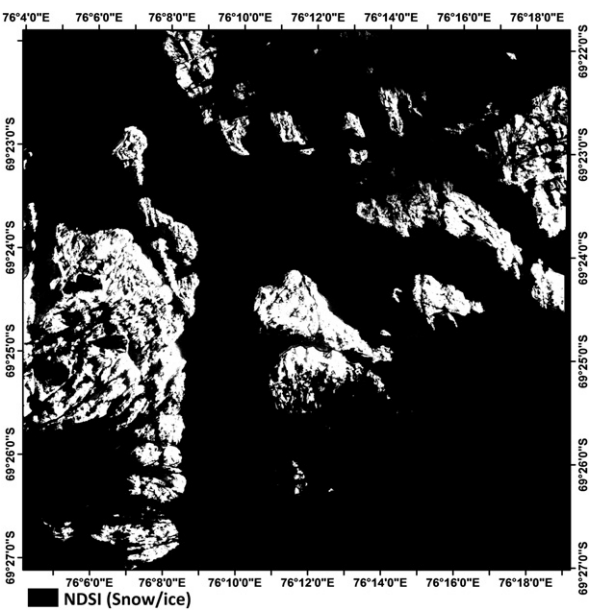

Fig. 8. Resultant merged NDSI map compiled from GS-sharpened image.

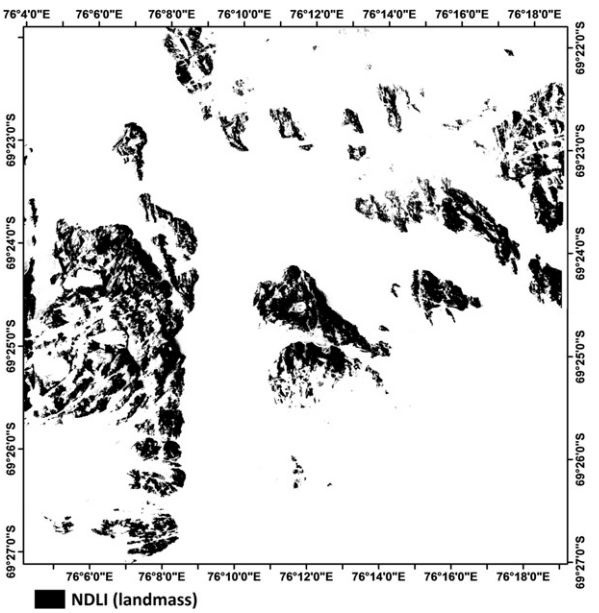

Fig. 9. Resultant merged NDLI map compiled from GS-sharpened image.

sharpened output (four combinations from each of NDVI, NDLI and NDWI) were merged using GIS operations to produce a final output map. Thus, our methodology yielded six final output maps from a total of 72 GIS layers using six pan-sharpening algorithms. The overall accuracy assessment of each land-cover map was carried out using 3000 stratified random points. Final accuracy assessment results of each land-cover map are expressed in terms of the widely used comprehensive measures, overall accuracy and the kappa ($\widehat{\boldsymbol{K}}$) coefficient. A sample error matrix for the land-cover map based on GS-sharpened imagery is given in Supplementary Table 2. The overall accuracy statistics are given in Table 6 as a function of pan-sharpening algorithm.

We now present the accuracy statistics for the six land-cover output maps from the six pan-sharpened images. The GS ($\widehat{\boldsymbol{K}} = 0.98$) and W-PC ($\widehat{\boldsymbol{K}} = 0.97$) pan-sharpening-based land maps have overall accuracy of 98.76% and 98.20%, respectively, while the PC ($\widehat{\boldsymbol{K}} = 0.97$) pan-sharpening-based land map has an accuracy of 98.16%. Note that these three methods have higher overall accuracy than the other three pan-sharpening methods. In addition to overall accuracy, $\widehat{\boldsymbol{K}}$, both the user's accuracy and producer's accuracy of GS-merged land-cover maps are much better than the others, which in turn proves the robustness of our accuracy assessment.

The overall trend of land-cover mapping accuracy for the six pan-sharpening methods can be summarized in terms of overall accuracy and kappa statistics as, GS > W-PC > PC > EF > BT > HPF, suggesting that the GS algorithm ($\widehat{\boldsymbol{K}} = 0.98$) performed best, while HPF ($\widehat{\boldsymbol{K}} = 0.96$) performed worst of the set of six algorithms (Fig. 10). Similar trends have been observed for all the measures of land-cover mapping accuracy derived from the error matrices. Note that the overall accuracies for the W-PC (98.20% and $\widehat{\boldsymbol{K}} = 0.97$) and PC (98.16% and $\widehat{\boldsymbol{K}} = 0.97$) algorithms were very similar, suggesting equivalent performance of these algorithms. Additionally, we present the results of the classification experiment on the original MSI (without pan-sharpening) to evaluate the mapping improvement achieved using pan-sharpening procedures. The statistics listed in Table 6 suggest that all the six pan-sharpened images performed much better than the original MSI, improving the mapping accuracy by approximately 2–3% in terms of overall accuracy, equivalent to an improvement of 0.02–0.04 in $\widehat{\boldsymbol{K}}$ value.

The error evaluation summarized in Table 7 indicates that the error of commission/inclusion (EC) is smallest for NDWI, ranging from 0.71% to 2.21% for the six pan-sharpening algorithms. This indicates that the smallest number of misclassified landmass or snow/ice pixels is included in the water class. However, the error of omission/exclusion (EO) for all six methods is greatest for NDWI. This implies that a significant percentage of water pixels ranging from 1.90% to 3.00% were misclassified as landmass or snow; the number was lowest for GS and highest for HPF. As for the NDLI, the GS method gave the lowest EO (0.70%) while BT (2.30%) scored the highest, indicating the lowest (highest) number of misclassifications of landmass pixel for GS (BT). We also note that EC values for NDLI are lowest for GS (1.59%) and highest for HPF (2.78%), giving the smallest (highest) amount of misclassification of water or snow pixels as landmass for GS (HPF). GS again performs the best for NDSI, with lowest values of EO (1.10%) and EC (1.40%). On the other hand, HPF performance was the worst in terms of EO (2.30%) and EF performed the worst in terms of EC (2.88%). The most significant observation in terms of overall EC and EO is that W-PC and PC had similar numbers of errors, suggesting comparable performance.

The producer's accuracy (PA) results are also summarized in Table 7. These indicate that for GS-sharpened images about 98.90% of snow/ice pixels,

Table 6
Overall accuracy statistics for all the resultant individual land cover maps.

Pan-sharpening method	Error matrix based accuracy (%)				Land cover area based accuracy		
	Overall accuracy	Kappa value	User's accuracy	Producer's accuracy	RMSE (m^2)	Misclassified pixels (No.)	%Bias
GS	98.76	0.98	98.77	98.77	2943.92	11776	3.62
W-PC	98.20	0.97	98.20	98.20	3559.03	14236	4.57
PC	98.16	0.97	98.17	98.17	8602.32	34409	10.12
EF	97.70	0.96	97.70	97.70	10801.23	43205	8.89
BT	97.56	0.96	97.57	97.57	15577.76	62311	18.05
HPF	97.50	0.96	97.50	97.50	17720.04	70880	22.75
MSI	95.14	0.94	95.13	95.16	85490.74	341963	15.03

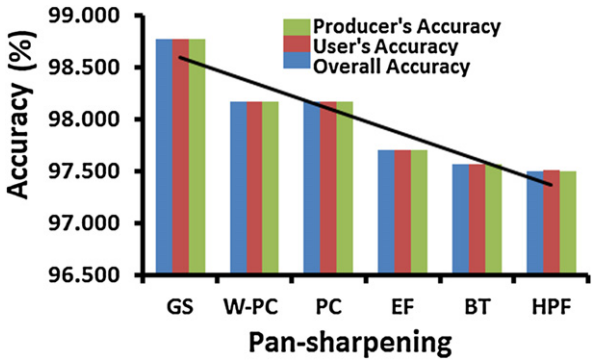

Fig. 10. Error matrix based classification accuracy statistics for six pan-sharpening methods. User's, producer's and overall accuracies are expressed in terms of percentage.

99.30% of landmass pixels, and 98.10% of water pixels were classified correctly, at their correct locations. In other words, 1.10% of snow pixels were omitted from NDSI and misclassified as either landmass or water, 0.70% of landmass pixels were omitted from NDLI and misclassified as snow or water, and 1.90% of water pixels were omitted from NDWI and misclassified as snow or landmass. The user's accuracy (UA) results summarized in Table 7 reveal that for GS-sharpened images about 98.60% of snow/ice pixels, 98.41% of landmass pixels, and 99.29% of water pixels were classified correctly, at their correct locations. In other words, 1.40% of landmass/water pixels were included in NDSI and misclassified as snow pixels, 1.59% of snow/water pixels were included in NDLI and misclassified as landmass, and 0.71% of snow/landmass pixels were included in NDWI and misclassified as water.

The above assessment of the results (Fig. 10) obtained from various SIRs of pan-sharpening methods suggests that the pan-sharpening methods GS, W-PC, and PC provided better results than the other methods, with the GS performing best. This implies that pan-sharpening using GS and W-PC methods had the minimum effect on subsequent processing of WV-2 data.

6.4. Comparative assessment of pan-sharpening methods on the basis of land-cover area based accuracy measures

We analyzed six pan-sharpening methods for their ability to support WV-2 based land-cover mapping. Overall accuracy statistics for all the resultant individual land-cover maps generated from six pan-sharpened images are summarized in Table 6. Data used for RMSE and bias calculation of pan-sharpened images using customized SIRs are summarized in Table 8. A positive (negative) bias indicates the average amount of underestimate (overestimate) in the extracted area. The RMSE was calculated to evaluate the error in total land-cover area extraction carried out by using various algorithms (Table 8). The number of misclassified pixels leads to an increase or decrease in the area of extracted land-cover. This in turn contributes to the overall RMSE. Thus, the RMSE is a measure of misclassification and hence the overall accuracy of land-cover extraction. Considering the 0.5 m resolution of the WV-2 pan-sharpened image, each misclassified pixel introduces 0.25 m^2 of RMSE in the extracted area. SIR-based measured areas are compared with reference areas in Fig. 11.

As RMSE is a more reliable and more representative measure of accuracy than the bias, we focus on the former. The performance of each algorithm can be ranked quantitatively using RMSE, and several quantitative inferences about their performance can be made. The overall trend of potential and accuracy of all the pan-sharpening methods for land-cover extraction can be summarized in terms of RMSE and number of misclassified pixels as GS > W-PC > PC > EF > BT > HPF, suggesting

Table 7
Error matrix based producer's and user's accuracy statistics.

Pan-sharpening	NDSI (Snow/Ice)				NDLI (Landmass)				NDWI (Water)			
	PA	EO	UA	EC	PA	EO	UA	EC	PA	EO	UA	EC
GS	98.90	1.10	98.60	1.40	99.30	0.70	98.41	1.59	98.10	1.90	99.29	0.71
W-PC	98.70	1.30	98.21	1.79	98.20	1.80	98.00	2.00	97.70	2.30	98.39	1.61
PC	98.70	1.30	98.21	1.79	98.20	1.80	97.91	2.09	97.60	2.40	98.39	1.61
EF	97.90	2.10	97.12	2.88	98.10	1.90	97.71	2.29	97.10	2.90	98.28	1.72
BT	97.80	2.20	97.51	2.49	97.70	2.30	97.41	2.59	97.20	2.80	97.79	2.21
HPF	97.70	2.30	97.21	2.79	97.80	2.20	97.22	2.78	97.00	3.00	98.08	1.92
MSI	95.70	4.30	94.40	5.60	95.28	4.72	95.80	4.20	94.50	5.50	95.20	4.80

Table 8
Land-cover area statistics for all resultant land-cover maps.

Reference data		SIR-based extracted/classified area (km^2) and bias (%)													
		GS		W-PC		PC		EF		BT		HPF		MSI	
Class	Area	Area	Bias	Area	Bias	Area	Bias	Area	Bias	Area	Bias	Area	Bias	Area	Bias
Water body	0.36	0.32	11.11	0.31	13.89	0.25	30.56	0.26	27.78	0.16	55.56	0.11	69.44	0.22	38.88
Landmass	12.96	12.99	−0.23	12.98	−0.15	12.97	−0.08	13.11	−1.16	13.14	−1.39	13.1	−1.08	11.99	7.48
Ice/Snow	86.68	86.69	−0.01	86.71	−0.03	86.78	−0.12	86.63	0.06	86.7	−0.02	86.79	−0.13	87.79	−1.28
Average		3.62		4.57		10.12		8.89		18.05		22.75		15.03	

that the GS algorithm performed best, with the lowest average RMSE in the set of six algorithms. In terms of percentage bias, the trend is almost the same except that EF performed better than PC. This anomaly results from a positive bias with snow/ice cover for EF, and a negative bias for PC. Note that EF is the only method that yielded a positive bias (underestimate) for snow/ice cover among the six pan-sharpening algorithms. Also note that all the pan-sharpening methods had a positive bias for water, and a negative bias for snow/ice and landmass, indicating that significant numbers of water pixels were misclassified as either landmass or snow/ice cover.

The GS-sharpened and W-PC-sharpened images performed better than the remaining pan-sharpened images for water body mapping (NDWI), with the lowest biases of 11.11% and 13.89%, respectively. PC-sharpened images performed best for landmass mapping (NDLI) with the lowest bias (−0.08%),

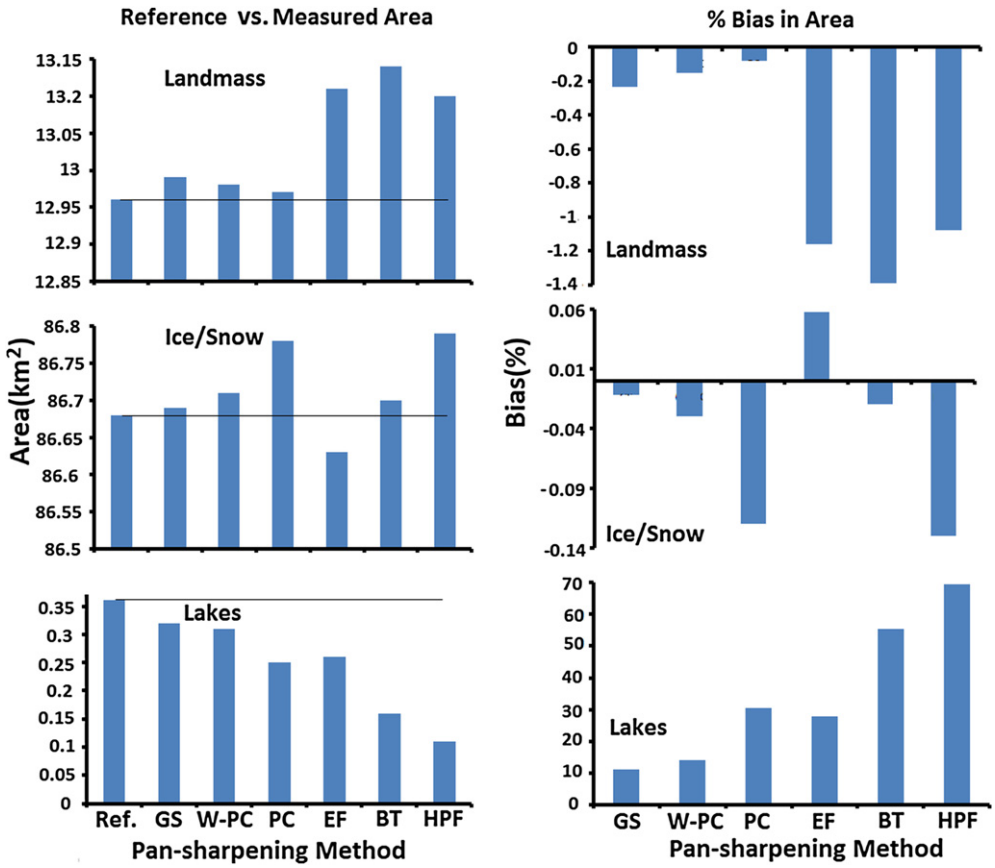

Fig. 11. Comparison between SIR-based land-cover class area and reference class (manually digitized) area in terms of bias (%).

followed closely by W-PC (−0.15%), while GS and BT demonstrated good performance for snow/ice (NDSI) with the lowest biases of −0.01% and −0.02%, respectively. In general, GS is the optimum sharpening algorithm for mapping water and snow while PC is ideal for landmass mapping. The performance of BT was more or less alike to GS for snow mapping. The representative accuracy of six land-cover maps is expressed in terms of RMSE. GS-sharpened images performed best with the lowest RMSE (2943.92 m^2), while HPF performed worst with the highest RMSE (17720.04 m^2). The GS-sharpened extracted final land-cover map is shown in Fig. 12.

Additionally, to test the robustness of our methodology, we compared the accuracy of the GS-sharpened land-cover map generated using one SIR combination against the final land-cover map generated using four SIR combinations. The $\widehat{K}$ index statistics for GS-sharpened land-cover maps generated with four SIR combinations and with a single SIR combination are given in Table 9. The land-cover map generated from using four SIR combinations had a $\widehat{K}$ value (0.98) significantly higher than for the land-cover map generated using one SIR combination (0.92). The result highlights the advantage of using multiple combinations of available bands to formulate SIRs, and their contribution to generating a final precise map.

7. Discussion

Our study differs from earlier work (Ben-Dor et al., 2001; Fernandez et al., 1997; Hall et al., 1995a; Huggel et al., 2002) in three key areas: (i) the use of 8-band data, (ii) the customization of SIRs, and (iii) the reconstruction of SIRs to yield an accurate land-cover map of the study area. The characteristic feature of this analysis is that, except for a few mixed pixels, no layers overlap in this land-cover, which indicates a high degree of accuracy in the resultant output map. Typically, where regions of classification are not set to reasonable thresholds, false signals do exist. However, false signals in this dataset have been almost completely mitigated for GS-sharpened images by the sequential optimization of a final threshold.

Most misclassifications in the SIR-based land-cover mapping procedure are related to three main types of error. (1) Inaccuracies due to cast shadow: there is a high probability that shadowed pixels are misclassified as water, unless a suitable correction is applied. The frequency and magnitude of these errors are closely linked to the topography of the study area. (2) Blue band saturation: Snow and ice have high

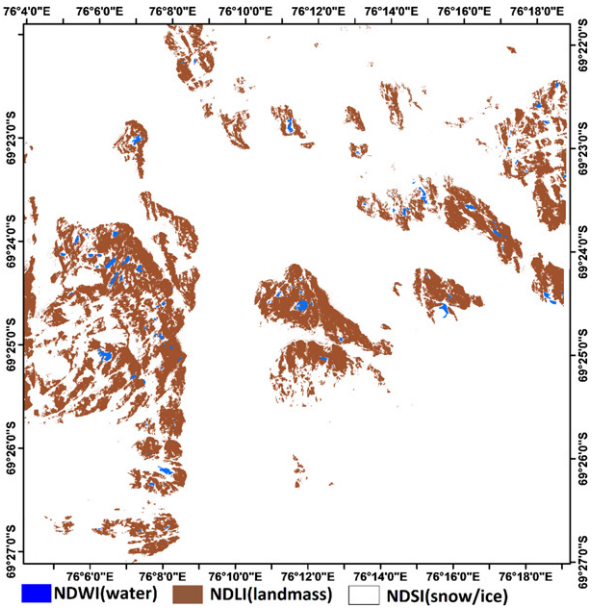

Fig. 12. Resultant SIR-based land-cover map compiled from GS-sharpened image.

reflectivity in the visible range of the electromagnetic spectrum. Sun glint effects for pixels with the relevant slope and aspect can saturate the blue band, leading to misclassification in both the "customized NDWI" and "customized NDLI". (3) The magnitude of the spectral distortion introduced by the pan-sharpening methods.

In order to reduce the cast shadow effect, a dark object subtraction (DOS) was applied to the blue channel (Crippen, 1988). This procedure, however, produced only minor improvements. Hence, for water surface extraction, the detected water areas need to be checked for shadow. Otherwise some water areas can be underestimated (overestimated) due to a false negative (positive) signal and may result in a positive (negative) bias. Negative bias was omnipresent and dominant for NDLI and NDSI, while positive bias was omnipresent for NDWI in all the pan-sharpening methods (Table 8), suggesting a misclassification of landmass and snow pixels and an underestimate of water pixels. The negative bias indicates that the extracted land-cover area is estimated to be larger than the original (reference) area.

Table 9
The kappa index ($\widehat{K}$) for GS-sharpened land-cover maps generated with four SIR combinations and with one SIR combination.

	Kappa index	
Pan-sharpening	Four SIR combinations	One SIR combination
Gram Schmidt	0.98	0.92

To provide a wider context to the study, we decided to utilize multiple combinations of available bands to generate SIR maps. Different band combinations enabled us to determine minute differences in the performance of the fusion and SIR procedures. It also provided a platform to gain insights into the role of specific spectral bands for the maximum extraction of information from the pan-sharpened products. The use of all combinations enabled us to carry out a wide variety of statistical analyses of the research experiment, which was very successful. However, we note that the present application is limited to polar regions, and may not represent the practicability and robustness of SIR-based land-cover mapping methods for urban areas, which are prone to variable shadow effect due to elevated manmade structures.

8. Conclusions

The combined use of all the SIRs, computed using the twin set of V−NIR bands, provided an accurate means for differentiating various land-cover classes. The magnitude of spectral and spatial distortions induced by pan-sharpening impacts on subsequent processing, which greatly affects the final accuracy of the analysis. The reduction of pan-sharpening-induced spectral distortions due to processing of 8-band acquisitions is attributed to the three major experimental superiorities: (i) use of multiple SIRs, (ii) optimum and constant thresholding for each set of customized SIRs, and (iii) synergistic merging of all SIR images to produce land-cover classes from the dataset.

We set out with the goals of covering a handful of uniquely customized SIRs to provide accurate spatial and spectral information for Antarctic land-cover mapping and fostering a new capability using WV-2 data. Our research provides new procedures to overcome the pan-sharpening-triggered spectral distortions of WV-2 imagery, and so will contribute to a better understanding of the earth's surface. The present work reinforces the view that the traditional pan-sharpening algorithms coupled with a wide array of SIRs from WV-2 data provide an effective tool for mapping the Antarctic surface.

Acknowledgments

We are indebted to "DigitalGlobe Inc. 8-band Research Challenge" which provided us with the research platform and the necessary images free of cost. We thank the Australian Antarctic Data Center for providing us with the supplementary GIS data layers for the study area. We are also grateful to Ms. Prachi Vaidya and Ms. Stephanie Grebas for their constructive comments on the draft version of the manuscript. Comments from two anonymous reviewers benefitted the paper. We acknowledge Mr. R. Ravindra, former Director NCAOR, for his encouragement and motivation of this research. This is NCAOR contribution no. 47/2012.

Appendix A. Supplementary data

Supplementary data related to this article can be found at http://dx.doi.org/10.1016/j.polar.2012.12.002.

References

Achard, F., Estréguil, C., 1995. Forest classification of Southeast Asia using NOAA AVHRR data. Remote Sens. Environ. 54, 198−208.

Alparone, L., Baronti, S., Garzelli, A., Nencini, F., 2004. A global quality measurement of pan-sharpened multispectral imagery. IEEE Geosci. Remote Sens. Lett. 1 (4), 313−317.

Alparone, L., Wald, L., Chanussot, J., Thomas, C., Gamba, P., Bruce, L.M., 2007. Comparison of pansharpening algorithms: outcome of the 2006 GRS-S data-fusion contest. IEEE Trans. Geosci. Remote Sens. 45 (10), 3012−3021.

Amro, I., Mateos, J., Vega, M., Molina, R., Katsaggelos, A.K., 2011. A survey of classical methods and new trends in pansharpening of multispectral images. EURASIP J. Adv. Signal. Process. 2011, 79.

Ben-Dor, E., Levin, N., Saaroni, H., 2001. A spectral based recognition of the urban environment using the visible and near-infrared spectral region (0.4−1.1 μm): a case study over Tel-Aviv. Int. J. Remote Sens. 22 (11), 2193−2218.

Bovolo, F., Bruzzone, L., Capobianco, L., Garzelli, A., Marchesi, S., 2010. Analysis of the effects of pansharpening in change detection on VHR images. IEEE Geosci. Remote Sens. Lett. 7 (1), 53−57.

Chavez, P.S., Sides, S.C., Anderson, J.A., 1991. Comparison of three different methods to merge multiresolution and multispectral data: landsat TM and SPOT panchromatic. Photogramm. Eng. Remote Sens 57 (3), 295−303.

Choi, M., 2006. A new intensity-hue-saturation fusion approach to image fusion with a tradeoff parameter. IEEE Trans. Geosci. Remote Sens. 44, 1672−1682.

Cliche, G., Bonn, F., Teillet, P., 1985. Integration of the SPOT panchromatic channel into its multispectral mode for image sharpness enhancement. Photogramm. Eng. Remote Sens. 51, 311−316.

Congalton, R.G., 1991. A review of assessing the accuracy of classifications of remotely sensed data. Remote Sens. Environ. 37, 35−46.

Crippen, R.E., 1988. The dangers of underestimating the importance of data adjustments in band rationing. Int. J. Remote Sens. 9 (4), 767−776.

Dozier, J., 1989. Spectral signature of alpine snow cover from the Landsat Thematic Mapper. Rem. Sens. Environ. 28, 9−22.

Ehlers, M., 1991. Multisensor image fusion techniques in remote sensing. ISPRS J. Photogramm. Remote Sens. 46 (1), 19−30.

Ehlers, M., 2008. Multi-image fusion in remote sensing: spatial enhancement vs. spectral characteristics preservation. In: Bebis, G., et al. (Eds.), Advances in Visual Computing Part II. Springer Verlag, Berlin, pp. 75−84.

Ehlers, M., Klonus, S., Astrand, P.J., Rosso, P., 2010. Multi-sensor image fusion for pansharpening in remote sensing. Int. J. Image Data Fusion 1 (1), 25–45.

ENVI 4.8, 2011. Exelis Visual Information Solutions, Image Sharpening Module, Boulder, Colorado. www.exelisvis.com.

ERDAS IMAGINE 9.3, 2010. Intergraph, Resolution Merge Module. http://geospatial.intergraph.com/Homepage.aspx.

Fernandez, A., Illera, P., Casanova, J.L., 1997. Automatic mapping of surfaces affected by forest fires in Spain using AVHRR NDVI composite image data. Remote Sens. Environ. 60, 153–162.

Gao, B.-C., 1996. NDWI: a normalized difference water index for remote sensing of vegetation liquid water from space. Remote Sens. Environ. 58, 257–266.

Hall, D.K., Foster, J.L., Chien, J.Y.L., Riggs, G.A., 1995a. Determination of actual snow-covered area using Landsat TM and digital elevation model data in Glacier National Park, Montana. Polar Rec. 31, 191–198.

Hall, D.K., Riggs, G.A., Salomonson, V.V., 1995b. Development of methods for mapping global snow cover using moderate resolution imaging spectroradiometer data. Remote Sens. Environ. 54, 127–140.

Hallada, W.A., Cox, S., 1983. Image sharpening for mixed spatial and spectral resolution satellite systems. In: Proc.. of the 17th International Symposium on Remote Sensing of Environment. University of Michigan, Ann Arbor, MI, pp. 1023–1032. 9–13 May.

Harris, U., 2008. Larsemann Hills – Mapping from Aerial Photography Captured February 1998. Australian Antarctic Data Centre CAASM Metadata. http://data.aad.gov.au/aadc/metadata/.

Huggel, C., Kaab, A., Haeberli, W., Teysseire, P., Paul, F., 2002. Remote sensing based assessment of hazards from glacier lake outbursts: a case study in the Swiss Alps. Can. Geotechnical J. 39, 316–330.

Klonus, S., Ehlers, M., 2007. Image fusion using the Ehlers spectral characteristics preservation algorithm. GIScience Remote Sens 44 (2), 93–116.

Kumar, U., Mukhopadhyay, C., Ramachandra, T.V., 2009. Pixel based fusion using IKONOS imagery. Int. J. Recent Trend Eng. 1 (1), 173–175.

Laben, C.A., Brower, B.V., 2000. Process for Enhancing the Spatial Resolution of Multispectral Imagery Using Pan-sharpening. US Patent 6,011,875.

Li, J., 2000. Spatial quality evaluation of fusion of different resolution images. ISPRS Int. Arch. Photogramm. Remote Sens XXXIII (B2–2), 339–346.

Li, Z., Jing, Z., Yang, X., Sun, S., 2005. Color transfer based remote sensing image fusion using non-separable wavelet frame transform. Pattern Recognit. Lett. 26 (13), 2006–2014.

Li, S., Li, Z., Gong, J., 2010. Multivariate statistical analysis of measures for assessing the quality of image fusion. Int. J. Image Data Fusion 1, 47–66.

McFeeters, S.K., 1996. The use of the Normalized Difference Water Index (NDWI) in the delineation of open water features. Int. J. Remote Sens. 17, 1425–1432.

Moser, G., Serpico, S.B., 2009. Unsupervised change detection from multichannel SAR data by Markovian data fusion. IEEE Trans. Geosci. Remote Sens. 47 (7), 2114–2128.

Otazu, X., Gonzalez-Audicana, M., Fors, O., Nunez, J., 2005. Introduction of sensor spectral response into image fusion methods. Application to wavelet-based methods. IEEE Trans. Geosci. Remote Sens. 43 (10), 2376–2385.

Padwick, C., Deskevich, M., Pacifici, F., Smallwood, S., 2010. WorldView 2 Pan-sharpening. In: Proceedings ASPRS 2010 Annual Conference. California, San Diego.

Pohl, C., Van Genderen, J.L., 1998. Multisensor image fusion in remote sensing: concepts, methods, and applications. Int. J. Remote Sens. 19 (5), 823–854.

Pradhan, P., King, R.L., Younan, N.H., Holcomb, D.W., 2006. Estimation of the number of decomposition levels for a wavelet-based multiresolution and multisensor image fusion. IEEE Trans. Geosci. Remote Sens. 44 (12), 3674–3686.

Ranchin, T., Wald, L., 2000. Fusion of high spatial and spectral resolution images: the ARSIS concept and its implementation. Photogramm. Eng. Remote Sens. 66 (1), 49–61.

Ranchin, T., Aiazzi, B., Alparone, L., Baronti, S., Wald, L., 2003. Image fusion—the ARSIS concept and some successful implementation schemes. ISPRS J. Photogramm. Remote Sens. 58, 4–18. http://dx.doi.org/10.1016/S0924-2716(03)00013-3.

Rouse, J.W., Haas, R.H., Schell, J.A., Deering, D.W., 1974. Monitoring vegetation systems in the Great Plains with ERTS. In: Proceedings of 3rd Earth Resource Technology Satellite (ERTS) Symposium, NASA, 309–317. http://ntrs.nasa.gov/archive/nasa/casi.ntrs.nasa.gov/19740022614_1974022614.pdf.

Schowengerdt, R.A., 1980. Reconstruction of multispatial, multispectral image data using spatial frequency content. Photogramm. Eng. Remote Sens. 46 (10), 1325–1334.

Shah, V.P., Younan, N.H., King, R.L., 2008. An efficient pan-sharpening method via a combined adaptive PCA approach and contourlets. IEEE Trans. Geosci. Remote Sens. 46 (5), 1323–1335.

Shi, W., Zhu, C., Tian, Y., Nichol, J., 2005. Wavelet-based image fusion and quality assessment. Int. J. Appl. Earth Observ. Geoinform. 6, 241–251.

Sidjak, R.W., Wheate, R.D., 1999. Glacier mapping of the Illecillewaet ice field, British Columbia, Canada, using Landsat TM and digital elevation data. Int. J. Remote Sens. 20, 273–284.

Thomas, C., Wald, L., 2007. Comparing Distances for Quality Assessment of Fused Images. In: Bochenek, Z. (Ed.), Proc. 26th EARSeL Annu. Symp. New Develop. Challenges Remote Sens. Warsaw, Poland, May 2006. Balkema, The Netherlands, pp. 101–111.

Thomas, C., Ranchin, T., Wald, L., Chanussot, J., 2008. Synthesis of multispectral images to high spatial resolution: a critical review of fusion methods based on remote sensing physics. IEEE Trans. Geosci. Remote Sens. 46 (5), 1301–1312.

Tso, B., Mather, P.M.C., 2001. Classification Methods for Remotely Sensed Data. Taylor and Francis, London.

Tucker, C.J., 1979. Red and photographic infrared linear combinations for monitoring vegetation. Remote Sens. Environ. 8, 127–150.

Updike, T., Comp, C., 2010. Radiometric Use of WorldView-2 Imagery. Technical Note. DigitalGlobe®, Colorado, USA [online]. Available from: www.digitalglobe.com/downloads/Radiometric_Use_of_WorldView-2_Imagery.pdf (accessed 04.10.11.).

Vijayaraj, V., Younan, N.H., O'Hara, C.G., 2006. Quantitative analysis of pansharpened images. Opt. Eng. 45 (4), 046202. http://dx.doi.org/10.1117/1.2195987.

Vrabel, J., Doraiswamy, P., McMurtrey, J., Stern, A., 2002. Demonstration of the accuracy of improved resolution hyperspectral imagery. SPIE Symp. Proc. 4725, 556–567.

Wald, L., January 26–28, 2000. Quality of high resolution synthesized images: is there a simple criterion? In: Ranchin, T., Wald, L. (Eds.), Proc. Int. Conf. Fusion Earth Data. Sophia Antipolis, France, pp. 99–103.

Wald, L., Ranchin, T., Mangolini, M., 1997. Fusion of satellite images of different spatial resolutions: assessing the quality of resulting images. Photogramm. Eng. Remote Sens 63 (6), 691–699.

Wang, Z., Bovik, A.C., 2002. A universal image quality index. IEEE Signal. Proc. Lett. 9 (3), 81–84.

Wang, Z., Bovik, A.C., Sheikh, H.R., Simoncelli, E.P., 2004. Image quality assessment: from error visibility to structural similarity. IEEE Trans. Image Process. 13 (4), 600–612.

Wang, Z., Ziou, D., Armenakis, C., Li, D., Li, Q., 2005. A comparative analysis of image fusion methods. IEEE Trans. Geosci. Remote Sens. 43 (6), 1391–1402.

Welch, R., Ehlers, M., 1987. Merging multiresolution SPOT HRV and Landsat TM data. Photogramm. Eng. Remote Sens. 53, 301–303.

Yuhendra, Alimuddin I., Sumantyo, J.T.S., Kuze, H., 2012. Assessment of pan-sharpening methods applied to image fusion of remotely sensed multi-band data. Int. J. Appl. Earth Observ. Geoinform. 18, 165–175. http://dx.doi.org/10.1016/j.jag.2012.01.013.

Yunhao, C., Lei, D., Jing, L., Xiaobing, L., Peijun, S., 2006. A new wavelet-based image fusion method for remotely sensed data. Int. J. Remote Sens. 27 (7), 1465–1476.

Zhang, Y., 2004. Highlight article: understanding image fusion. Photogramm. Eng. Remote Sens. 70 (6), 657–661.

Zhang, Y., 2008. Methods for image fusion quality assessment – a review, comparison and analysis. ISPRS Int. Arch. Photogramm. Remote Sens. XXXVII (B7), 1101–1110.

Zhou, J., Civco, D.L., Silander, J.A., 1998. A wavelet transform method to merge Landsat TM and SPOT panchromatic data. Int. J. Remote Sens. 19 (4), 743–757.